nature materials

Article

https://doi.org/10.1038/s41563-023-01547-8

Real-space observation of ultraconfined in-plane anisotropic acoustic terahertz plasmon polaritons

Received: 23 November 2022

Accepted: 31 March 2023

Published online: 4 May 2023

Check for updates

S. Chen[1,2,14], P. L. Leng[3,14], A. Konečná[4,5], E. Modin[2], M. Gutierrez-Amigo[6,7], E. Vicentini[2], B. Martín-García[2,8], M. Barra-Burillo[2], I. Niehues[2], C. Maciel Escudero[2,6], X. Y. Xie[3], L. E. Hueso[2,8], E. Artacho[2,8,9,10], J. Aizpurua[6,10], I. Errea[6,10,11], M. G. Vergniory[10,12], A. Chuvilin[2,8], F. X. Xiu[3] ✉ & R. Hillenbrand[8,13] ✉

Thin layers of in-plane anisotropic materials can support ultraconfined polaritons, whose wavelengths depend on the propagation direction. Such polaritons hold potential for the exploration of fundamental material properties and the development of novel nanophotonic devices. However, the real-space observation of ultraconfined in-plane anisotropic plasmon polaritons (PPs)—which exist in much broader spectral ranges than phonon polaritons—has been elusive. Here we apply terahertz nanoscopy to image in-plane anisotropic low-energy PPs in monoclinic Ag_2Te platelets. The hybridization of the PPs with their mirror image—by placing the platelets above a Au layer—increases the direction-dependent relative polariton propagation length and the directional polariton confinement. This allows for verifying a linear dispersion and elliptical isofrequency contour in momentum space, revealing in-plane anisotropic acoustic terahertz PPs. Our work shows high-symmetry (elliptical) polaritons on low-symmetry (monoclinic) crystals and demonstrates the use of terahertz PPs for local measurements of anisotropic charge carrier masses and damping.

Polaritons are electromagnetic waves formed by strong coupling between light and dipolar matter excitations such as plasmons, phonons or excitons[1]. They attract wide attention due to their ability to confine and guide light at the nanometre scale, promising the development of ultrasmall resonators and waveguides for sensing, heat transfer and optical circuitry applications[2–8]. The control and manipulation of polaritons can be largely expanded with naturally anisotropic materials, as the strong light confinement can be accompanied by

[1]Terahertz Technology Innovation Research Institute, National Basic Science Center—Terahertz Science and Technology Frontier, Terahertz Precision Biomedical Discipline 111 Project, Shanghai Key Lab of Modern Optical System, University of Shanghai for Science and Technology, Shanghai, China. [2]CIC nanoGUNE BRTA, Donostia-San Sebastián, Spain. [3]State Key Laboratory of Surface Physics and Department of Physics, Institute for Nanoelectronic Devices and Quantum Computing, Zhangjiang Fudan International Innovation Center, Fudan University, Shanghai, China. [4]Central European Institute of Technology, Brno University of Technology, Brno, Czech Republic. [5]Institute of Physical Engineering, Brno University of Technology, Brno, Czech Republic. [6]Materials Physics Center, CSIC-UPV/EHU, Donostia-San Sebastián, Spain. [7]Departamento de Física, Facultad de Ciencia y Tecnología, Universidad del País Vasco (UPV/EHU), Bilbao, Spain. [8]IKERBASQUE, Basque Foundation for Science, Bilbao, Spain. [9]Theory of Condensed Matter, Cavendish Laboratory, University of Cambridge, Cambridge, UK. [10]Donostia International Physics Centre (DIPC), Donostia-San Sebastián, Spain. [11]Departamento de Física Aplicada, Escuela de Ingeniería de Gipuzkoa, Universidad del País Vasco (UPV/EHU), Donostia-San Sebastián, Spain. [12]Max Planck for Chemical Physics of Solids, Dresden, Germany. [13]CIC nanoGUNE BRTA and Department of Electricity and Electronics, UPV/EHU, Donostia-San Sebastián, Spain. [14]These authors contributed equally: S. Chen, P. L. Leng. ✉e-mail: faxian@fudan.edu.cn; r.hillenbrand@nanogune.eu

https://doi.org/10.1038/s41563-023-01547-8

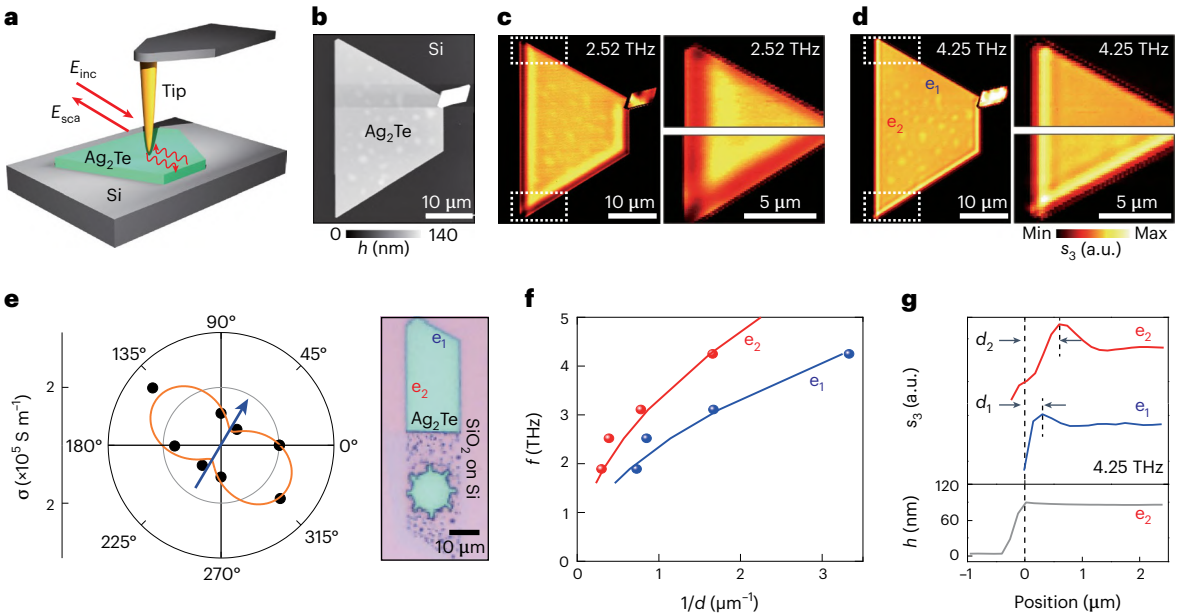

Fig. 1 | Real-space nanoimaging of in-plane anisotropic THz PPs on Ag_2Te platelets. a, Illustration of the polariton imaging experiment. Here E_{inc} and E_{sca} indicate the illuminating and tip-scattered field, respectively. The sine waves on the platelet indicate the tip-launched and edge-reflected PPs, respectively. **b**, Topography image of an 85-nm-thick Ag_2Te platelet on Si. **c**, Near-field image (left) of the whole platelet at 2.52 THz. Enlarged views (right) of the platelet corners marked by the dashed white rectangles (left). **d**, Same as **c** but for 4.25 THz. **e**, Directional in-plane electrical transport measurements of a Ag_2Te platelet on a SiO_2/Si substrate. Light microscopy image (right) of a Ag_2Te platelet, whose lower part was etched to obtain a disc with small rectangular protrusions serving as the contact pads. The black dots show the directional in-plane conductivity that was measured between two diametrically opposed electrodes through the four-terminal method (left). The brown solid curve shows the fit described in Supplementary Note 3. The blue arrow marks the direction perpendicular to edge e_1. **f**, Qualitative dispersion of PPs propagating perpendicular to the platelet edges marked e_1 and e_2 in **d**, obtained by plotting the frequency f versus $1/d_1$ (blue dots) and $1/d_2$ (red dots). Here d_1 and d_2 were extracted from the near-field line profiles (such as the ones shown in **g**) across the platelet edges e_1 and e_2. The solid lines are guides to the eye. **g**, Near-field line profiles across the platelet edges e_1 and e_2, extracted from the near-field image at 4.25 THz (shown in **c**). The bottom graph shows the topography (that is, height h) profile across the e_2 edge. The vertical dashed line marks the platelet edge. Here d_1 and d_2 are the distances between the platelet edge and the respective first near-field signal maximum.

negative phase velocities, highly directional propagation or exotic wavefront shapes[3,7–19].

When a polaritonic material exhibits optical anisotropy along its surface, polaritons can propagate with ultrashort and direction-dependent wavelengths, promising unprecedented pathways for nanoscale guiding and manipulation of electromagnetic energy. Recently, in-plane anisotropic phonon polaritons (PhPs) were observed in natural polar materials such as α-MoO_3 (refs. 12–14), α-V_2O_5 (ref. 16), $CaCO_3$ (ref. 17) and β-GaO (ref. 7). They exhibit ultralong lifetimes of up to several picoseconds, yielding long polariton propagation lengths despite their strongly compressed wavelength compared with the corresponding free-space photon wavelength. On the other hand, the existence of PhPs is limited to rather narrow spectral ranges between the transverse and longitudinal optical phonon frequencies (Reststrahlen bands)[20].

Compared with PhPs, plasmon polaritons (PPs) in semiconductors and semimetals offer the advantage of being available in much broader spectral ranges and being tunable by doping. PPs with in-plane anisotropic properties were predicted for black phosphorous[21] and borophene[22,23] and observed by far-field spectroscopy of black phosphorus carbide[24] and tungsten telluride PP resonators[25]. However, the experimental visualization of propagating in-plane anisotropic PPs—particularly over several wavelengths and at frequencies of a few terahertz (THz)—has been elusive so far.

Ultraconfined PPs often suffer from larger damping and shorter propagation length compared with PhPs, with PP lifetimes often being below 0.6 ps (refs. 26–29). In the technologically increasingly important THz spectral range, such lifetimes correspond to about one temporal oscillation cycle of the THz field. Although such times are large enough for the development of ultrasmall plasmonic THz resonators[25,30], the propagation length of ultraconfined PPs in thin layers is in the range of the polariton wavelength or less[28,29,31,32], challenging their real-space observation and potential on-chip circuitry applications.

Here we use scattering-type scanning near-field optical microscopy (s-SNOM) (refs. 26,27) to image ultraconfined in-plane anisotropic THz PPs on monoclinic Ag_2Te (hessite) platelets. Ag_2Te is a narrow-bandgap semiconductor with electron concentrations of around 10^{18} cm^{-3} at room temperature, where the effective masses of the charge carriers exhibit strong anisotropy[33–35]. We enhance the confinement and relative propagation length of the PPs by hybridizing them with their mirror image in an adjacent metal substrate, yielding acoustic plasmon polaritons (APPs). Most importantly, the anisotropy of polariton propagation is qualitatively retained and the long APP propagation lengths reveal an elliptical APP isofrequency contour in the wavevector space. By crystal structure analysis using scanning transmission electron microscopy (STEM), we can explain the highly symmetric (elliptical) polariton propagation along the low-symmetry crystal. We finally demonstrate how the elliptical APPs can be exploited for measuring in-plane anisotropic effective carrier masses.

Single-crystalline Ag_2Te platelets were grown on sapphire by chemical vapour deposition[35] (Methods) and transferred onto different substrates. As illustrated in Fig. 1a, we performed polariton interferometry using s-SNOM (Methods and Supplementary Note 1)[26,27]. A metallized atomic force microscopy tip is illuminated with p-polarized THz radiation of frequency f, concentrating the incident field at its very apex to a nanoscale THz hot spot that excites polaritons propagating radially away from the tip. When the polaritons are reflected at the platelet edges, recording of the tip-scattered THz field as a function

https://doi.org/10.1038/s41563-023-01547-8

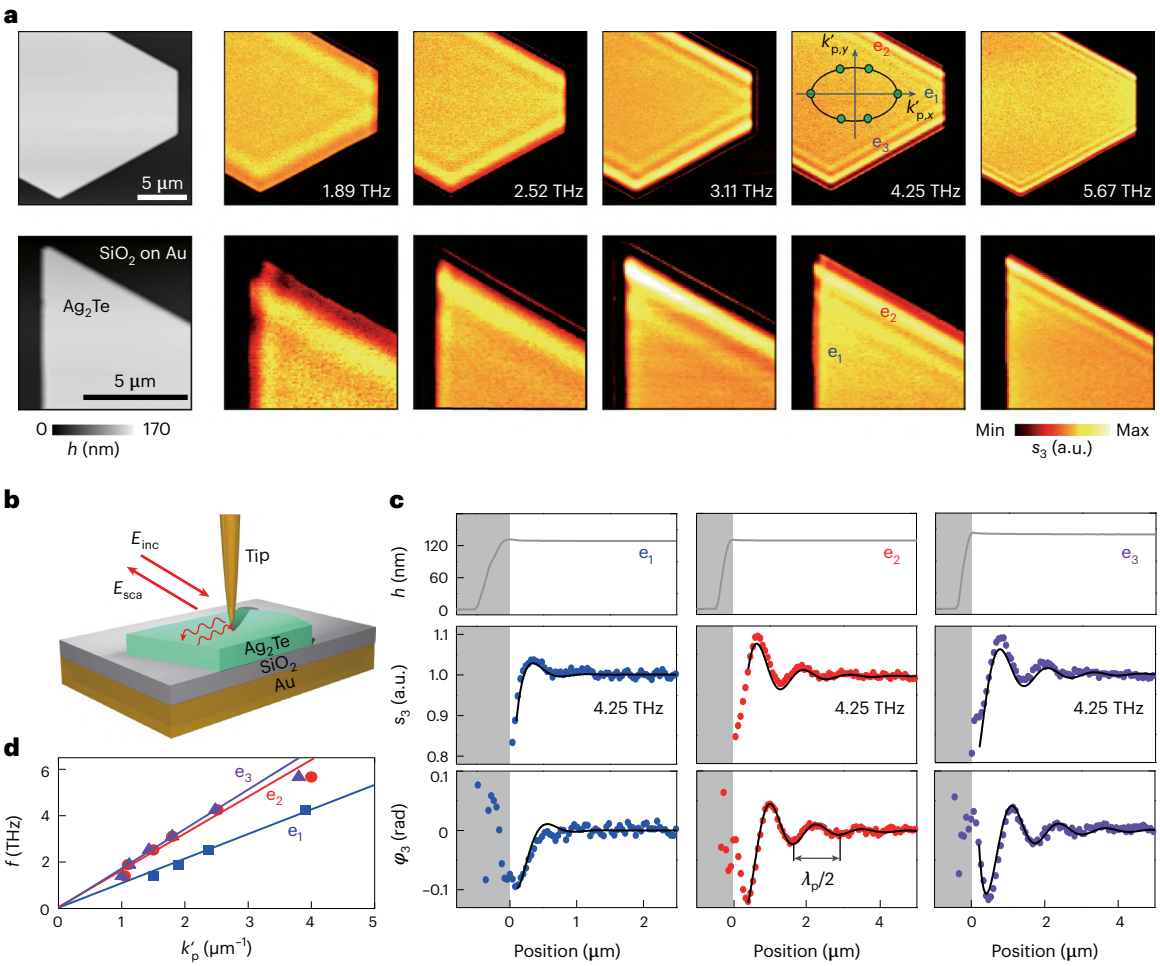

Fig. 2 | Real-space nanoimaging of in-plane anisotropic THz APPs on a Ag_2Te/SiO_2/Au heterostructure. a, Topography (grey-scale images) and THz near-field images of different parts of one Ag_2Te platelet. The images were recorded with a Au-coated tip with 250 nm apex radius. In the centre of the near-field image at 4.25 THz, we show an in-plane wavevector diagram, where the green dots show the real part of the APP wavevector perpendicular to the edges e_1, e_2 and e_3. The black solid line represents an ellipse. **b**, Illustration of the s-SNOM experiment (analogous to Fig. 1a) with a sample comprising $h = 135$-nm-thick Ag_2Te platelet on top of a $t = 52$-nm-thick SiO_2 layer on top of a 50-nm-thick Au film. **c**, Line profiles across (perpendicular to) the edges e_1, e_2 and e_3, showing the topography, near-field amplitude s_3 and near-field phase φ_3 at 4.25 THz. The positions of 0 nm correspond to the platelet edges. The grey and white background marks the substrate and platelet area, respectively. The black solid lines show fits to the experimental data with a radially propagating damped wave. **d**, APP dispersion perpendicular to the platelet edges e_1 (blue), e_2 (red) and e_3 (violet). The symbols represent the experimental values obtained from fitting near-field amplitude and phase line profiles for different frequencies, as illustrated in Fig. 2c for 4.25 THz. The solid lines are linear guides to the eye.

of tip position yields images of polariton interference fringes with a spacing of typically half the polariton wavelength, that is, $\lambda_p/2$.

We first imaged an 85-nm-thick Ag_2Te platelet on a Si substrate, whose topography is shown in Fig. 1b. In the THz near-field images (Fig. 1c,d), we observe a bright fringe parallel to the platelet edges, which is a typical observation for polaritons with short propagation lengths[29,36]. These fringes can be better appreciated in the THz near-field line profiles (Fig. 1g) across the edges e_1 and e_2 (Fig. 1c,d), where maxima of the near-field signal (corresponding to the fringes) can be clearly seen at distances d_1 and d_2 to the platelet edges. Plotting the frequency f versus $1/d_i$, the latter representing a qualitative proxy for the real part of the polariton wavevector, $k'_{p,i} = 2\pi/\lambda_{p,i}$ (ref. 36), we observe a strong increase of $1/d_i$ with increasing f, which is a typical characteristic of a polariton dispersion (Fig. 1f). Most interestingly, the fringes parallel to edge e_1 are much narrower and closer to the edge than the fringes parallel to edge e_2, indicating $k'_{p,1} > k'_{p,2}$ and thus a strongly anisotropic in-plane PP dispersion.

To gain further insights, we conducted in-plane directional electrical transport measurements on a Ag_2Te disc with multiple contact pads (Methods and Supplementary Note 2). We found a strongly anisotropic electrical conductivity with the lowest conductivity nearly perpendicular to platelet edge e_1, indicating that the polariton anisotropy is related to in-plane anisotropic electronic properties.

The relative propagation length of the polaritons, L/λ_p, is rather short, challenging the measurement of the polariton wavelength λ_p and polariton dispersion. As discussed elsewhere[37,38], one can increase L/λ_p by placing the layer that supports polaritons onto a thin dielectric layer on top of a metal surface (Methods), such that acoustic polaritons (also referred to as image polaritons[38,39]) are formed. The coupling of the polaritons with their mirror image in the metal surface has the advantages that λ_p is reduced and an exceptional strong field concentration inside the spacer can be achieved[5,28,37,38,40]. We adopted this idea and placed a Ag_2Te platelet onto a thin SiO_2 layer on a Au layer (Fig. 2). The THz near-field images of the Ag_2Te/SiO_2/Au heterostructure reveal up to three narrow polariton fringes parallel to the edges e_2 and e_3 (Fig. 2a), contrary to only one fringe observed on the platelets on Si (Fig. 1c,d). Importantly, the polariton wavelength (that is, fringe spacing and width) still depends on the propagation direction (similar to theoretical predictions for other APPs[41,42]) and is smaller for the polaritons propagating perpendicular to edge e_1.

https://doi.org/10.1038/s41563-023-01547-8

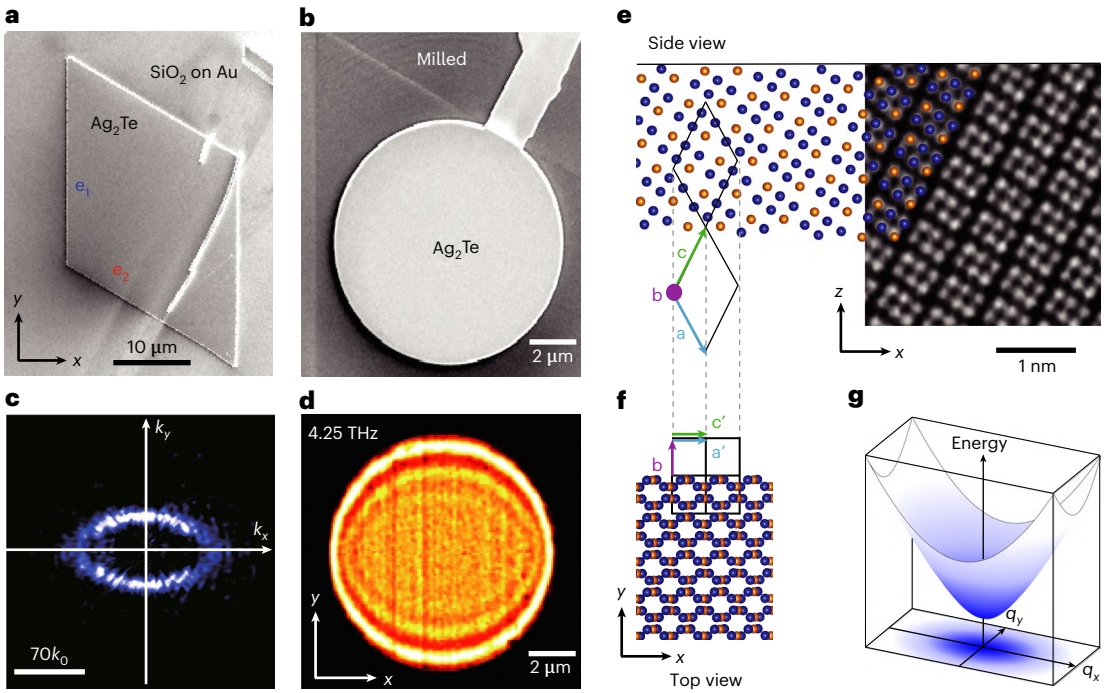

Fig. 3 | Relationship between anisotropic APP propagation, platelet geometry and crystal lattice structure. a, Scanning electron microscopy image of a 135-nm-thick Ag_2Te platelet on top of a 17-nm-thick SiO_2 layer on top of an Au layer. **b**, Scanning electron microscopy image of a Ag_2Te disc, which was obtained by focused-ion-beam milling of the Ag_2Te platelet (shown in **a**). **c**, Fourier transform of the THz near-field images shown in **d**. **d**, Near-field image of the Ag_2Te disc shown in **b**, recorded at 4.25 THz. Image processing (described in Supplementary Note 5) was applied for better visibility of the polariton fringes. **e**, STEM (grey-scale) image of a cross section of a Ag_2Te platelet. The cross section is oriented perpendicular to the Ag_2Te platelet's monoclinic unit-cell axis shown in **b**, which is parallel to the platelet surface. The blue and orange dots represent the Ag and Te atoms of the monoclinic Ag_2Te (hessite) crystal structure (ID: mp-1592; space group: $P2_1/c$ (no. 14); point group: C_{2h} (2/*m*)) and were matched to the STEM image. The arrows labelled **a**, **b** and **c** represent the unit-cell vectors. **f**, Top view of the crystal structure. The arrows labelled **a**′ and **c**′ represent the projection of the corresponding unit-cell vectors onto the *x*–*y* plane (surface plane). **g**, Band structure of Ag_2Te in the *x*–*y* plane, showing the electron energy as a function of electron momentum in the *x* and *y* directions, q_x and q_y, respectively.

For a better understanding of the APPs, we recorded amplitude- and phase-resolved THz near-field line profiles across the platelet edges e_1, e_2 and e_3 (marked in the 4.25 THz image; Fig. 2a). Complex-valued fitting of both amplitude s_3 and phase φ_3 line profiles (established elsewhere[29] and shown in Fig. 2c) with a radially propagating damped wave yields the complex-valued polariton wavevectors $k_{p,i}$ perpendicular to edges e_i (Methods and Supplementary Note 3). The real part of the wavevectors, $k'_{p,i}$ (green dots), is shown in the wavevector diagram plotted in the centre of the near-field image at 4.25 THz (Fig. 2a), indicating an elliptical isofrequency contour (solid line), which could originate from an in-plane anisotropic effective electron mass in Ag_2Te, an in-plane anisotropic high-frequency permittivity or both (discussed hereafter).

To determine the polariton dispersion, $\omega\left(k'_{p,i}\right)$, we recorded the amplitude- and phase-resolved THz near-field line profiles across the platelet edges e_1, e_2 and e_3 at various frequencies *f* and fitted them analogously to Fig. 2c. We find a nearly linear polariton dispersion for the lower frequencies (Fig. 2d), which is a typical characteristic of acoustic modes. From the slopes, we find large PP wavelength compressions (relative to the photon wavelength λ_0) of about $\lambda_{p,1}/\lambda_0 \approx 1/42$, $\lambda_{p,2}/\lambda_0 \approx 1/27$ and $\lambda_{p,3}/\lambda_0 \approx 1/27$, providing experimental evidence of ultraconfined anisotropic APPs.

Surprisingly, the elliptical isofrequency curve indicates a rather high-symmetry APP propagation, which cannot be straightforwardly connected to the non-orthogonal platelet edges and the low-symmetry monoclinic crystal structure of Ag_2Te. Indeed, a recent study of PhPs on monoclinic β-phase Ga_2O_3 reports the emergence of shear polaritons featuring tilted wavefronts and asymmetric polariton responses[7,8], which we did not observe in Figs. 1 and 2. We clarify this observation in the following by establishing a geometric connection between the APP propagation and the crystal structure of Ag_2Te.

We first verified the elliptical isofrequency curve and its main axes. To that end, we fabricated (Supplementary Note 4) a disc (Fig. 3b) from one $Ag_2Te/SiO_2/Au$ heterostructure (Fig. 3a), such that all the APP directions can be probed. The THz near-field image at 4.25 THz (Fig. 3d) reveals more than two interference fringes all around the disc circumference. Their spacing has a minimum in the *x* direction (perpendicular to edge e_1) and continuously increases to reach its maximum in the *y* direction (which is non-orthogonal to any of the platelet edges). Fourier transform of the image (Supplementary Note 5) confirms the elliptical isofrequency contour (Fig. 2a). In contrast to Fig. 2, we now see more than two interference fringes in all the propagation directions and that the fringe spacing is reduced. This further compression of the polariton wavelength (up to $\lambda_p/\lambda_0 \approx 1/65$) was achieved by reducing the thickness of the SiO_2 spacer from 52 to 17 nm, that is, by increasing the coupling between platelet PPs and their image in the Au surface.

To understand the relationship between the main axes of the elliptical isofrequency contour and the crystal structure of the Ag_2Te platelets, we took a STEM image of a platelet cross section (Fig. 3e,f, grey-scale image) that is oriented perpendicular to platelet edge e_1 (Supplementary Note 6). In Fig. 3e,f, the arrangement of atoms (white dots) can be well matched by the crystal structure of monoclinic Ag_2Te (blue and orange dots represent Ag and Te atoms, respectively) when the unit-cell vector **b** (the one being orthogonal to both **a** and **c** axes) is oriented parallel to the platelet surface and edge e_1. The vector **b** is thus orthogonal to the projections of the unit-cell vectors **a** and **c** onto the platelet surface, **a**′ and **c**′, respectively, which explains the high-symmetry elliptical isofrequency contour (Fig. 3c) and its

https://doi.org/10.1038/s41563-023-01547-8

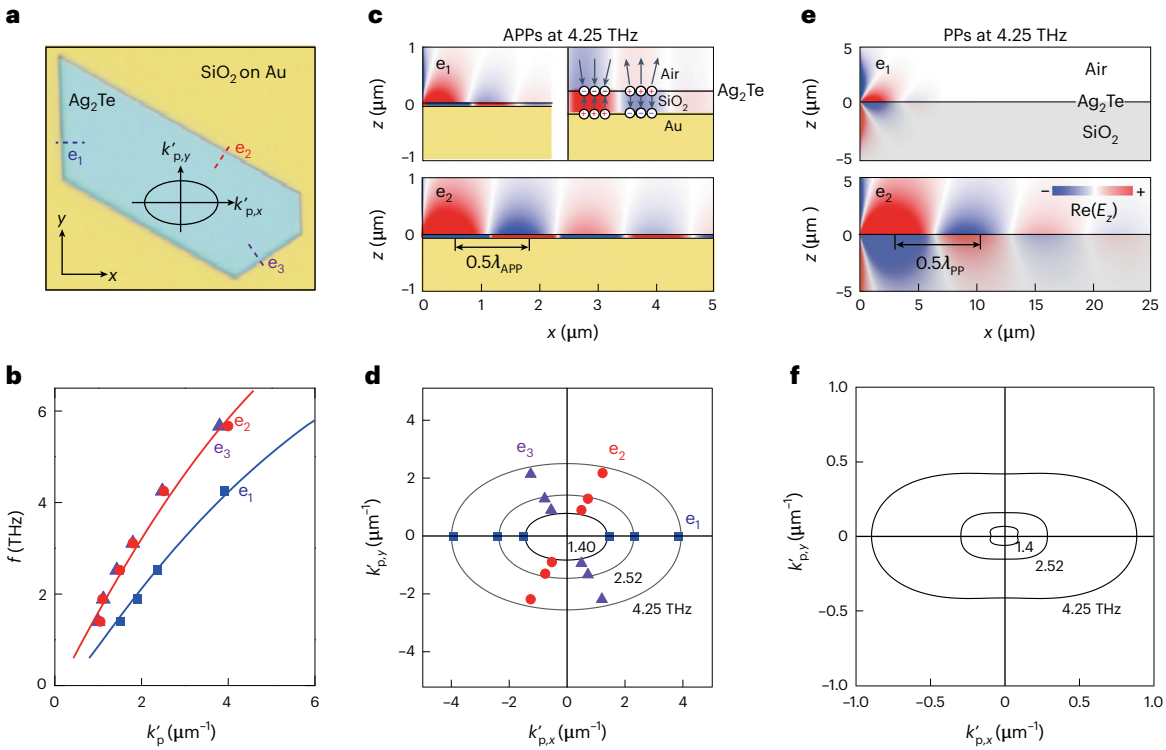

Fig. 4 | PP dispersions and isofrequency curves. a, Light microscopy image of the Ag_2Te platelet on a SiO_2 thin layer on Au, which is discussed in Fig. 2. The diagram shows the isofrequency contour of the APPs. **b**, APP dispersion perpendicular to the platelet edges e_1 (blue), e_2 (red) and e_3 (violet), as obtained from the near-field line profiles recorded along the dashed lines in **a**. The symbols show the experimental data of Fig. 2d. The solid lines show the fits described in the main text. **c**, Calculated near-field distribution (real part of vertical electric field, $\mathrm{Re}(E_z)$) of APPs at 4.25 THz, which propagate radially and perpendicular to platelet edges e_1 and e_2 (top and bottom, respectively). The 135-nm-thick platelet on a 52-nm-thick SiO_2 layer on Au is described as a 2D sheet with a conductivity obtained from the fit of the APP dispersion in **b**. The right side shows a zoomed-in view into the spacer region, illustrating the charges in the Ag_2Te sheet, image charges in the Au surface and associated electric field distribution. **d**, Solid lines show the calculated isofrequency contours of APPs. The material parameters are the same as in **c**. The symbols show the experimental data of **b**. **e**, Calculated near-field distribution (real part of the vertical electric field, $\mathrm{Re}(E_z)$) of radially propagating PPs at 4.25 THz, which propagate perpendicular to platelet edges e_1 and e_2 (top and bottom, respectively). The 135-nm-thick platelet on top of SiO_2 is described and shown as a 2D sheet with conductivity obtained from the fit of the PP dispersion of **b**. **f**, Calculated isofrequency contours of PPs. The material parameters are the same as in **e**.

orientation, and thus the high-symmetry yet anisotropic PP propagation. For other crystal orientations, for which the projections of the unit-cell vectors onto the platelet surface were non-orthogonal, shear polaritons may be observed[7,8].

Based on the Ag_2Te crystal structure and its orientation, we performed first-principles calculations of the two-dimensional (2D) electronic band structure parallel to the platelet surface (Fig. 3g and Supplementary Note 7). The band structure can be well approximated by an elliptical paraboloid with the minimum at the Γ point, which allows for describing the electronic properties and dielectric function of the Ag_2Te platelets by an anisotropic Drude model. For a quantitative analysis of the experimental polariton dispersions and isofrequency contours, we thus model the Ag_2Te platelet as a layer of zero thickness[43,44] that is characterized by an anisotropic sheet (2D) conductivity as

$$\hat{\sigma}(\omega) = \mathrm{i}\omega\varepsilon_0 h(\hat{\mathrm{I}} - \hat{\varepsilon}(\omega)), \tag{1}$$

where $\hat{\varepsilon}(\omega)$ is a 2×2 anisotropic permittivity tensor describing the surface plane of the Ag_2Te platelet, $\hat{\mathrm{I}}$ is the identity tensor, ε_0 is the vacuum permittivity and $\omega = 2\pi f$. Since the projection of the unit cell onto the platelet surface is orthogonal (Fig. 3e), the tensors $\hat{\varepsilon}(\omega)$ and $\hat{\sigma}(\omega)$ are diagonal in the x–y coordinate system (Fig. 3a). According to the Drude model, the diagonal permittivity tensor elements can be described as

$$\varepsilon_{xx}(\omega) = \varepsilon_{\mathrm{IR},x} - \frac{\omega_{\mathrm{p},x}^2}{\omega^2 + \mathrm{i}\gamma_x\omega} \text{ and } \varepsilon_{yy}(\omega) = \varepsilon_{\mathrm{IR},y} - \frac{\omega_{\mathrm{p},y}^2}{\omega^2 + \mathrm{i}\gamma_y\omega}, \tag{2}$$

where $\varepsilon_{\mathrm{IR},i}\,(i = x, y)$ are the directional high-frequency (infrared) permittivities of Ag_2Te, γ_i is the directional charge carrier damping (inverse of the carrier scattering time) and

$$\omega_{\mathrm{p},i} = 2\pi f_{\mathrm{p},i} = \sqrt{\frac{ne^2}{m_{\mathrm{eff},i}\varepsilon_0}} \tag{3}$$

is the (unscreened) directional plasma frequencies with $m_{\mathrm{eff},i}$ being the directional effective carrier masses, n being the carrier concentration, and e being the electron charge. Considering further that the conductivity sheet is located on a thin dielectric spacer on a perfect metal conductor (representing the Au surface), we obtain an analytical description of the dispersion relation of the in-plane anisotropic APPs (Supplementary Note 8), which we can use to simultaneously fit the experimentally measured polariton dispersions $\omega(k_{\mathrm{p},i})$ using $\omega_{\mathrm{p},i}$, γ_i and $\varepsilon_{\mathrm{IR},x}$ as fit parameters and setting $\varepsilon_{\mathrm{IR},y} \approx 1.9\varepsilon_{\mathrm{IR},x}$ and $(\varepsilon_{\mathrm{IR},x} + \varepsilon_{\mathrm{IR},y})/2 = 11$ (derived from s-SNOM imaging of Ag_2Te platelets at mid-infrared frequencies; Supplementary Notes 9–11).

We apply the theoretical description above to analyse (Fig. 4) the experimental polariton data shown in Fig. 2d. In Fig. 4a, we show the whole Ag_2Te platelet and indicate by the dashed lines where the THz

near-field amplitude and phase line profiles were measured, yielding the APP dispersions shown in Fig. 4b (symbols, corresponding to the data of Fig. 2d). We achieved an excellent fitting of the polariton dispersions (Fig. 4b, solid lines) for $f_{p,x} = 28.9$ THz, $f_{p,y} = 44.4$ THz, $\gamma_x = 2.4$ THz and $\gamma_y = 0.9$ THz, confirming the nearly linear dispersion that is characteristic for APPs. We use the fit parameters to calculate (Supplementary Note 8) and theoretically compare the electric field (vertical component $\mathrm{Re}(E_z)$) distribution and isofrequency curves of the APPs (Fig. 4c,d) and PPs in Ag_2Te platelets on a semi-infinite SiO_2 substrate (Fig. 4e,f). We obtain elliptical isofrequency contours for both APPs and PPs, which confirms that the propagation anisotropy is qualitatively preserved after the hybridization of the PPs with their mirror image in the Au substrate (Fig. 4c,d). The calculated field profiles further confirm the increased relative propagation length of the APPs, and that their wavevectors and field confinement are substantially enhanced compared with that of PPs, that is, the APP wavelength and field decay in the vertical (z) direction are strongly reduced (Fig. 4c,e). A zoomed-in view into the field distribution of APPs (Fig. 4c, right) also confirms the highly concentrated electric field inside the SiO_2 spacer, which is formed by the charges in the Ag_2Te platelet and their mirror images in the Au surface. We note that our theory can also be applied when the 2D conductivity tensor of a thin layer above a metal surface is non-diagonal. In this case, we expect acoustic shear polaritons, where both in-plane anisotropy and shearing properties are qualitatively retained.

APP interferometry can be applied to measure the anisotropic effective carrier mass both optically and at room temperature. We find $m_{\mathrm{eff},x}/m_{\mathrm{eff},y} = f_{p,y}^2/f_{p,x}^2 \approx 2.4$, which we attribute to the in-plane anisotropic band structure of the Ag_2Te platelets[33,45]. To obtain the effective carrier masses, we performed Hall measurements of the carrier concentration in one of the Ag_2Te platelets, yielding $n \approx 1.65 \times 10^{18}\,\mathrm{cm}^{-3}$ (Supplementary Note 12). Using equation (3), we obtain $m_{\mathrm{eff},x} \approx 0.16 m_e$ and $m_{\mathrm{eff},y} \approx 0.07 m_e$, where m_e is the electron mass, matching well with the values from the literature[33,35,46] and our band structure calculations, $m_{\mathrm{eff},x} \approx 0.18 m_e$ and $m_{\mathrm{eff},y} \approx 0.06 m_e$, respectively (Supplementary Note 7). We note that the carrier damping is anisotropic too ($\gamma_x = 2.4$ THz and $\gamma_y = 0.9$ THz), resulting in anisotropic relative APP propagation lengths (Fig. 2c) and APP amplitude decay times of $\tau_{\mathrm{APP},x} = 0.14$ ps and $\tau_{\mathrm{APP},y} = 0.31$ ps. A quantitative comparison with transport measurements corroborates our results (Methods). We note that Ag_2Te is a topological insulator[33,35,46], but we could explain the THz polariton dispersion exclusively by massive bulk carriers due to their dominance at room temperature[35]. In the future, low-temperature s-SNOM (ref. 47) could be employed for exploring potential topological in-plane anisotropic THz APPs.

In summary, we observed in-plane anisotropic PPs in the monoclinic semiconductor Ag_2Te by real-space THz nanoimaging. We found that their confinement and relative propagation length can be increased through the fabrication of Ag_2Te/spacer/metal heterostructures, whereas the in-plane anisotropic propagation characteristic remains. These in-plane anisotropic APPs manifest multiple spatial signal oscillations even for polariton amplitude decay times as short as about 0.2 ps, which—from a general perspective—is critically important for exploiting in-plane anisotropic PPs for future on-chip circuitry applications or for room-temperature measurements of in-plane materials properties such as directional effective charge carrier masses and charge carrier damping. The strong field concentration of APPs, particularly in the gap between the polaritonic layer and metal surface, may be exploited for field-enhanced molecular sensing or for boosting (ultra)strong THz light–matter coupling with molecules[48], classical 2D electron gases[49] or quantum materials.

Online content

Any methods, additional references, Nature Portfolio reporting summaries, source data, extended data, supplementary information, acknowledgements, peer review information; details of author contributions and competing interests; and statements of data and code availability are available at https://doi.org/10.1038/s41563-023-01547-8.

References

1. Basov, D. N., Asenjo-Garcia, A., Schuck, P. J., Zhu, X. & Rubio, A. Polariton panorama. *Nanophotonics* **10**, 549–577 (2020).
2. Daniel, R. et al. Mid-infrared plasmonic biosensing with graphene. *Science* **349**, 165–168 (2015).
3. Basov, D. N., Fogler, M. M. & Garcia de Abajo, F. J. Polaritons in van der Waals materials. *Science* **354**, aag1992 (2016).
4. Tielrooij, K. J. et al. Out-of-plane heat transfer in van der Waals stacks through electron–hyperbolic phonon coupling. *Nat. Nanotechnol.* **13**, 41–46 (2018).
5. Lee, I. H., Yoo, D., Avouris, P., Low, T. & Oh, S. H. Graphene acoustic plasmon resonator for ultrasensitive infrared spectroscopy. *Nat. Nanotechnol.* **14**, 313–319 (2019).
6. Bylinkin, A. et al. Real-space observation of vibrational strong coupling between propagating phonon polaritons and organic molecules. *Nat. Photon.* **15**, 197–202 (2020).
7. Passler, N. C. et al. Hyperbolic shear polaritons in low-symmetry crystals. *Nature* **602**, 595–600 (2022).
8. Hu, G. et al. Real-space nanoimaging of hyperbolic shear polaritons in a monoclinic crystal. *Nat. Nanotechnol.* **18**, 64–70 (2023).
9. Dai, S. et al. Tunable phonon polaritons in atomically thin van der Waals crystals of boron nitride. *Science* **343**, 1125–1129 (2014).
10. Caldwell, J. D. et al. Sub-diffractional volume-confined polaritons in the natural hyperbolic material hexagonal boron nitride. *Nat. Commun.* **5**, 5221 (2014).
11. Yoxall, E. et al. Direct observation of ultraslow hyperbolic polariton propagation with negative phase velocity. *Nat. Photon.* **9**, 674–678 (2015).
12. Zheng, Z. et al. Highly confined and tunable hyperbolic phonon polaritons in van der Waals semiconducting transition metal oxides. *Adv. Mater.* **30**, e1705318 (2018).
13. Ma, W. et al. In-plane anisotropic and ultra-low-loss polaritons in a natural van der Waals crystal. *Nature* **562**, 557–562 (2018).
14. Zheng, Z. et al. A mid-infrared biaxial hyperbolic van der Waals crystal. *Sci. Adv.* **5**, eaav8690 (2019).
15. Caldwell, J. D. et al. Photonics with hexagonal boron nitride. *Nat. Rev. Mater.* **4**, 552–567 (2019).
16. Taboada-Gutierrez, J. et al. Broad spectral tuning of ultra-low-loss polaritons in a van der Waals crystal by intercalation. *Nat. Mater.* **19**, 964–968 (2020).
17. Ma, W. et al. Ghost hyperbolic surface polaritons in bulk anisotropic crystals. *Nature* **596**, 362–366 (2021).
18. Zhang, Q. et al. Interface nano-optics with van der Waals polaritons. *Nature* **597**, 187–195 (2021).
19. Wu, Y. et al. Manipulating polaritons at the extreme scale in van der Waals materials. *Nat. Rev. Phys.* **4**, 578–594 (2022).
20. Low, T. et al. Polaritons in layered two-dimensional materials. *Nat. Mater.* **16**, 182–194 (2017).
21. Low, T. et al. Plasmons and screening in monolayer and multilayer black phosphorus. *Phys. Rev. Lett.* **113**, 106802 (2014).
22. Lian, C. et al. Integrated plasmonics: broadband Dirac plasmons in borophene. *Phys. Rev. Lett.* **125**, 116802 (2020).
23. Torbatian, Z., Novko, D. & Asgari, R. Hyperbolic plasmon modes in tilted Dirac cone phases of borophene. *Phys. Rev. B* **104**, 075432 (2021).
24. Huang, X. et al. Black phosphorus carbide as a tunable anisotropic plasmonic metasurface. *ACS Photon.* **5**, 3116–3123 (2018).
25. Wang, C. et al. Van der Waals thin films of WTe_2 for natural hyperbolic plasmonic surfaces. *Nat. Commun.* **11**, 1158 (2020).
26. Chen, J. N. et al. Optical nano-imaging of gate-tuneable graphene plasmons. *Nature* **487**, 77–81 (2012).

27. Fei, Z. et al. Gate-tuning of graphene plasmons revealed by infrared nano-imaging. *Nature* **487**, 82–85 (2012).
28. Alonso-Gonzalez, P. et al. Acoustic terahertz graphene plasmons revealed by photocurrent nanoscopy. *Nat. Nanotechnol.* **12**, 31–35 (2017).
29. Chen, S. et al. Real-space nanoimaging of THz polaritons in the topological insulator Bi_2Se_3. *Nat. Commun.* **13**, 1374 (2022).
30. Ju, L. et al. Graphene plasmonics for tunable terahertz metamaterials. *Nat. Nanotechnol.* **6**, 630–634 (2011).
31. Soltani, A. et al. Direct nanoscopic observation of plasma waves in the channel of a graphene field-effect transistor. *Light.: Sci. Appl.* **9**, 97 (2020).
32. Pogna, E. A. A. et al. Mapping propagation of collective modes in Bi_2Se_3 and $Bi_2Te_{2.2}Se_{0.8}$ topological insulators by near-field terahertz nanoscopy. *Nat. Commun.* **12**, 6672 (2021).
33. Zhang, W. et al. Topological aspect and quantum magnetoresistance of β-Ag_2Te. *Phys. Rev. Lett.* **106**, 156808 (2011).
34. Yeh, T.-T. et al. The optical properties of Ag_2Te crystals from THz to UV. *J. Alloys Compd.* **725**, 433–440 (2017).
35. Leng, P. et al. Gate-tunable surface states in topological insulator β-Ag_2Te with high mobility. *Nano Lett.* **20**, 7004–7010 (2020).
36. Dai, S. et al. Phonon polaritons in monolayers of hexagonal boron nitride. *Adv. Mater.* **31**, e1806603 (2019).
37. Menabde, S. G. et al. Real-space imaging of acoustic plasmons in large-area graphene grown by chemical vapor deposition. *Nat. Commun.* **12**, 938 (2021).
38. Menabde, S. G., Heiden, J. T., Cox, J. D., Mortensen, N. A. & Jang, M. S. Image polaritons in van der Waals crystals. *Nanophotonics* **11**, 2433–2452 (2022).
39. Lee, I. H. et al. Image polaritons in boron nitride for extreme polariton confinement with low losses. *Nat. Commun.* **11**, 3649 (2020).
40. Autore, M. & Hillenbrand, R. What momentum mismatch? *Nat. Nanotechnol.* **14**, 308–309 (2019).
41. Lee, I.-H. et al. Anisotropic acoustic plasmons in black phosphorus. *ACS Photon.* **5**, 2208–2216 (2018).
42. Lyu, W. et al. Anisotropic acoustic phonon polariton-enhanced infrared spectroscopy for single molecule detection. *Nanoscale* **13**, 12720–12726 (2021).
43. Gomez-Diaz, J. S., Tymchenko, M. & Alu, A. Hyperbolic plasmons and topological transitions over uniaxial metasurfaces. *Phys. Rev. Lett.* **114**, 233901 (2015).
44. Nikitin, A. Y. in *World Scientific Handbook of Metamaterials and Plasmonics. Recent Progress in the Field of Nanoplasmonics* Vol. 4 (ed Aizpurua, J.) (World Scientific, 2017).
45. Sulaev, A. et al. Experimental evidences of topological surface states of β-Ag_2Te. *AIP Adv.* **3**, 032123 (2013).
46. Lee, S. et al. Single crystalline β-Ag_2Te nanowire as a new topological insulator. *Nano Lett.* **12**, 4194 (2012).
47. Ni, G. X. et al. Fundamental limits to graphene plasmonics. *Nature* **557**, 530–533 (2018).
48. Damari, R. et al. Strong coupling of collective intermolecular vibrations in organic materials at terahertz frequencies. *Nat. Commun.* **10**, 3248 (2019).
49. Scalari, G. et al. Ultrastrong coupling of the cyclotron transition of a 2D electron gas to a THz metamaterial. *Science* **335**, 1323–1326 (2012).

Methods

Growth of Ag_2Te platelets and transfer onto different substrates

High-quality Ag_2Te platelets were grown by chemical vapour deposition using polycrystalline powder as the precursor and argon as the carrier gas[35]. The furnace was rapidly heated up to the growth temperature (in the range of 950–1,050 °C) within 20 min, held constant for 60 min and then naturally cooled with the flow of argon. The precursor was placed in the hot centre of the furnace. The *c*-cut sapphire substrates were put downstream.

The chemical-vapour-deposition-grown Ag_2Te platelets were transferred onto various substrates (Si, SiO_2 layer on Si, and thin SiO_2 layer on 50 nm Au layer on Si) using a polydimethylsiloxane-based dry-transfer method[50]. For the four-terminal electrical transport measurements, we used commercial silicon substrates covered with a 285-nm-thick SiO_2 layer (Bonda Technology). The SiO_2 layer on Au on Si substrates was fabricated as follows. First, a Cr layer of about 5 nm thickness was deposited by magnetron sputtering as an adhesion layer onto a Si substrate. Subsequently, a 50-nm-thick Au layer was sputtered onto the Cr layer. Finally, SiO_2 was sputtered onto the Au layer.

THz near-field microscopy setup

We used a THz s-SNOM, which is based on a commercial setup from Attocube AG, where a metallized atomic force microscopy tip acts as a THz near-field probe (Supplementary Fig. 1). The tip is illuminated with monochromatic THz radiation from a gas laser (SIFIR-50, Coherent), which is focused with a parabolic mirror. Via the lightning rod effect, the tip concentrates the THz radiation onto a nanoscale near-field spot at the tip apex. The tip-scattered field is recorded as a function of tip position. The collection and detection of the tip-scattered field are done with the same parabolic mirror and a cryogen-free THz Bolometer System (QMC Instruments). To obtain background-free near-field signals, the tip is oscillated at the cantilever's mechanical resonance frequency Ω (tapping mode) and the bolometer signal is demodulated at the third harmonic of the oscillation frequency, that is, 3Ω. To increase the signal-to-noise ratio, we used commercial Au tips with a large apex radius of about 250 nm (LRCH, Team Nanotec). They were oscillated at a frequency of about $\Omega \approx 70$ kHz with an amplitude of about 150 nm.

The near-field images (Figs. 1c,d, 2a and 3d) were obtained by recording the tip-scattered field with a Michelson interferometer, where the reference mirror was fixed at a position where the near-field signal on the Ag_2Te platelet was the maximum.

The near-field amplitude and phase line profiles (Fig. 2c and Supplementary Fig. 3), s_3 and φ_3, were obtained by synthetic optical holography[29,51–53], which is based on a Michelson interferometer where the reference mirror (mounted on a delay stage) is translated at a constant velocity along the reference beam path. The interferometric detection is the key to enable a complex-valued analysis of near-field profiles, which is critical for a reliable measurement of the wavelength of polaritons with short propagation lengths.

Four-terminal electrical transport measurements

To measure the directional in-plane conductivity of a Ag_2Te platelet (Fig. 1e), we first fabricated a circle-shaped nanoplatelet with contact pads via electron-beam lithography and ion beam etching with argon for 3–5 min. The electrodes were fabricated by electron-beam lithography, magnetron sputtering of Cr and Au (5 and 100 nm thickness, respectively) and lift-off. We then performed four-terminal electrical transport measurements[54], which allows for eliminating the contact resistance of the interface between the Au layer and platelet surface (Supplementary Fig. 2). To that end, we generated an electrical current (marked by a white arrow labelled I_i in Supplementary Fig. 2) through two diametrically opposed contact pads (labelled C_{I1} and C_{I2} in Supplementary Fig. 2) and measured the voltage V_{ii} between the two adjacent contact pads C_{V1} and C_{V2}. The index i stands for the direction defined by the diametrically opposed contact pads through which the current I_i flows. We obtained the resistance $R_{ii} = V_{ii}/I_i$, yielding the conductivity $\sigma_i = (R_{ii}hw/l)^{-1}$, where h and w are the thickness and diameter of the Ag_2Te disc, respectively. Here l is the distance between C_{V1} and C_{V2}. Using $w/l = \sqrt{2}$ and $h = 100$ nm for Ag_2Te discs, we obtained the in-plane directional conductivity (Fig. 1e).

The brown solid curve in Fig. 1e shows a fit by $\sigma_{max}\cos^2(\theta - \Phi) + \sigma_{min}\sin^2(\theta - \Phi)$ (ref. 55), where σ_{max} and σ_{min} are the maximum and minimum values of the sample conductivity, respectively. θ presents the directional angle where the sample conductivity is measured; and Φ is the angle relative to the reference angle (here the horizontal direction).

Relative propagation length and decay times of polaritons

The relative propagation length of polaritons is given by $L/\lambda_p = k_p' v_g \tau/(2\pi)$, where $L = 1/k_p''$ is the polariton propagation length, $v_g = d\omega/dk_p'$ is the group velocity and k_p'' is the imaginary part of the complex-valued polariton wavevector $k_p = k_p' + ik_p''$. We thus find $L/\lambda_p \propto k_p' v_g$, showing that L/λ_p can be increased by increasing k_p' but maintaining a large v_g. Because of the linear dispersion of acoustic modes, the increase in k_p' comes along with a much smaller reduction in v_g compared with increasing k_p' of non-acoustic polaritons. Consequently, L/λ_p is increased by turning polaritons in a thin layer into acoustic polaritons by placing the layer on top of a dielectric spacer on top of a metal surface.

The amplitude decay time of the polaritons can be calculated according to $\tau = L/v_g$ once their propagation lengths L and dispersion $\omega(k_p)$ are known. We obtained both of them by fitting the THz near-field line profiles to determine $\omega(k_p') = k_p' + ik_p''$, as described below.

Measurement of complex-valued polariton wavevectors

To measure the complex-valued polariton wavevector $k_{p,i} = k_{p,i}' + ik_{p,i}''$, where index i indicates the propagation direction, we recorded THz near-field amplitude and phase line profiles, $s_3(\xi)$ and $\varphi_3(\xi)$, respectively, across the edges e_1, e_2 and e_3 of the Ag_2Te platelet (Fig. 2a). Here ξ is the position relative to the edge of the Ag_2Te platelet. Each panel in Supplementary Fig. 3 shows the topography line profile (top left) and near-field amplitude and phase line profiles (symbols in middle and bottom left, respectively) across one edge at one THz frequency. The near-field amplitude and phase line profiles were normalized to the complex-valued signal C that is measured far away from the edge.

We obtained $k_{p,i}$ by complex-valued fitting of the near-field line profiles, as established in another work[29]. To that end, we constructed complex-valued line profiles, $\sigma_3(\xi) = s_3(\xi)e^{i\varphi_3(\xi)}$, and fitted them by

$$E_p = Ae^{i2k_{p,i}\xi}/\sqrt{2\xi} + C, \quad (4)$$

which describes the electric field of a back-reflected, radially (that is, tip-launched) propagating damped wave (Supplementary Fig. 3, black curves). The fitting parameters are A, $k_{p,i}$ and C. The real part of $k_{p,i}$ is shown by the symbols in Figs. 2d and 4b.

Preparation of sample cross section and STEM analysis

The STEM image (Fig. 3e) was obtained from a transmission electron microscopy lamella prepared by a standard focused-ion-beam lift-out technique (using a Helios 600 Nanolab dual-beam system) from the Ag_2Te platelet (Supplementary Fig. 6). The orientation of the lamella (marked by the red line) is perpendicular to the platelet surface and parallel to the x axis (perpendicular to edge e_1), as defined in Fig. 3. From an s-SNOM image recorded at 4.25 THz (colour-scale image; Supplementary Fig. 6) where we can clearly identify edge e_1, it was determined where the polariton fringes are more closely spaced.

STEM imaging has been performed on a Titan 60-300 (S)TEM instrument equipped with an x-FEG field emission gun and a retractable high-angle annular dark-field STEM detector at 300 kV accelerating

voltage. The optimal beam convergence semi-angle for these conditions was 10 mrad.

Comparison of anisotropic carrier properties with polariton interferometry and electrical transport measurements

To corroborate the anisotropic carrier properties, we use the effective carrier masses and carrier damping to calculate the d.c. conductivity according to $\sigma_{\mathrm{d.c.},i} = ne^2/(\gamma_i m_{\mathrm{eff},i})$. We obtain $\sigma_{\mathrm{d.c.},x} \approx 1.3 \times 10^5\,\mathrm{S\,m^{-1}}$ and $\sigma_{\mathrm{d.c.},y} \approx 5.7 \times 10^5\,\mathrm{S\,m^{-1}}$, which differ by only a factor of two from the transport measurements shown in Fig. 1e. We attribute this discrepancy to different charge carrier concentrations n in the different Ag_2Te platelets that were used for the electrical transport measurements and polariton interferometry. On the other hand, most importantly, the ratio between the conductivities in the y and x direction—which is a consequence of the anisotropy of effective mass and damping—is nearly the same in the transport ($\sigma_{\mathrm{d.c.},x}/\sigma_{\mathrm{d.c.},y} = 0.75 \times 10^5/3.08 \times 10^5 \approx 0.24$) and polariton interferometry ($\sigma_{\mathrm{d.c.},x}/\sigma_{\mathrm{d.c.},y} \approx 0.21$) measurements.

Data availability

Data that support the results of this work are available from the corresponding authors upon reasonable request.

References

50. Wang, L. et al. One-dimensional electrical contact to a two-dimensional material. *Science* **342**, 614–617 (2013).
51. Schnell, M., Carney, P. S. & Hillenbrand, R. Synthetic optical holography for rapid nanoimaging. *Nat. Commun.* **5**, 3499 (2014).
52. Maissen, C., Chen, S., Nikulina, E., Govyadinov, A. & Hillenbrand, R. Probes for ultrasensitive THz nanoscopy. *ACS Photon.* **6**, 1279–1288 (2019).
53. Chen, C. et al. Terahertz nanoimaging and nanospectroscopy of chalcogenide phase-change materials. *ACS Photon.* **7**, 3499–3506 (2020).
54. Lohmann, T., Klitzing, K. V. & Smet, J. H. Four-terminal magneto-transport in graphene p-n junctions created by spatially selective doping. *Nano Lett.* **9**, 1973–1979 (2009).
55. Zhong, M. et al. In-plane optical and electrical anisotropy of 2D black arsenic. *ACS Nano* **15**, 1701–1709 (2021).

Acknowledgements

The work was financially supported by the Spanish Ministry of Science and Innovation under the María de Maeztu Units of Excellence Program (CEX2020-001038-M/MCIN/AEI/10.13039/501100011033) (R.H., A.C., L.E.H. and E.A.); Projects PID2021-123949OB-I00 (R.H.), PID2019-109905GB-C21 (M.G.V. and I.E.), RTI2018-094861-B-100 (L.E.H.), PID2019-107432GB-I00 (J.A.) and PID2019-107338RB-C61 (E.A.) funded by MCIN/AEI/10.13039/501100011033 and by 'ERDF—A Way of Making Europe'; the National Natural Science Foundation of China (NSFC) (52225207 and 11934005) and the Shanghai Pilot Program for Basic Research—Fudan University 21TQ1400100 (21TQ006) (F.X.X.); NSFC grant no. 61988102 and the Science and Technology Commission of Shanghai Municipality (nos. 23010503400 and 23ZR1443500) (S.C.); the Czech Science Foundation GACR under the Junior Star grant no. 23-05119M (A.K.); the European Research Council (ERC) under grant agreement no. 101020833 (M.G.V.); the German Research Foundation (DFG) under project nos. 467576442 (I.N.) and GA 3314/1-1–FOR 5249 (QUAST) (M.G.V.); the Gipuzkoa Council (Spain) in the frame of the Gipuzkoa Fellows Program (B.M.-G.); and the University groups of the Basque Government (IT1526-22) (J.A.).

Author contributions

R.H. and S.C. conceived the study. P.L.L. and X.Y.X. fabricated the Ag_2Te platelets and performed the electrical transport and Hall measurements under the supervision of F.X.X. S.C. performed the THz s-SNOM imaging and related data analysis. A.K. developed the theoretical description of polariton modes and performed the dispersion fitting. E.V. performed the infrared PhP interferometry and related data analysis. A.C. fabricated the Ag_2Te disc. E.M. and A.C. performed the STEM analysis. M.G. performed the ab initio calculations under the supervision of I.E. and M.G.V. B.M.-G. participated in the crystal structure characterization and discussions. M.B.-B. and I.N. participated in the sample preparation. C.M.E., E.A., L.E.H. and J.A. participated in the theory discussions. R.H., S.C. and A.K. wrote the manuscript with input from all the authors. R.H. supervised the work.

Competing interests

R.H. was a co-founder of Neaspec GmbH, which now is a part of Attocube AG, a company producing s-SNOM systems, such as the one used in this study. The remaining authors declare no competing interests.

Additional information

Supplementary information The online version contains supplementary material available at https://doi.org/10.1038/s41563-023-01547-8.

Correspondence and requests for materials should be addressed to F. X. Xiu or R. Hillenbrand.

Peer review information *Nature Materials* thanks Joshua Caldwell, Ido Kaminer and Sang-Hyun Oh for their contribution to the peer review of this work.